Polymorphism and Structural Filiations in Five New Organic–Inorganic Hybrid Salts of the Heteroleptic Cationic Iridium(III) Complex and Polyoxometalates

Patricia Bolle, Hélène Serier-Brault, Amandine Boulmier, Marin Puget, Clotilde Menet, Olivier Oms, Jerome Marrot, Pierre Mialane, Anne Dolbecq, Remi Dessapt

Polymorphism and Structural Filiations in Five New Organic-inorganic Hybrid Salts of the Heteroleptic Cationic Iridium(III) Complex and Polyoxometalates

Patricia Bolle,[†] Hélène Serier-Brault,[†] Amandine Boulmier,[‡] Marin Puget,[†] Clotilde Menet,[†] Olivier Oms,[‡] Jérôme Marrot,[‡] Pierre Mialane,[‡] Anne Dolbecq,[‡] and Rémi Dessapt*[†]*

[†] Institut des Matériaux Jean Rouxel, Université de Nantes, CNRS, 2 rue de la Houssinière, BP 32229, 44322 Nantes, France.

[‡] Institut Lavoisier de Versailles, UMR 8180, Université de Versailles Saint-Quentin en Yvelines, Université Paris Saclay, 45 Avenue des Etats-Unis, 78035 Versailles Cedex, France.

ABSTRACT:

Five new hybrid compounds ionically associating the phosphorescent heteroleptic cationic iridium(III) complex $[Ir^{III}(ppy)_2(bpy)]^+$ ($[Ir]^+$) (ppy = 2-phenylpyridine, bpy = 2,2'-bipyridine) and anionic polyoxometalates (POMs) units have been successfully elaborated, namely $[Ir]_2[W_6O_{19}]\cdot H_2O$ (***m*-Ir$_2$W$_6$**), $[Ir]_2[W_6O_{19}]$ (***t*-Ir$_2$W$_6$-2**), $[Ir]_2[Mo_6O_{19}]$ (***t*-Ir$_2$Mo$_6$-2**), $[Ir]_4[\alpha\text{-}Mo_8O_{26}]\cdot 4DMF\cdot 5H_2O$ (**Ir$_4$αMo$_8$DMF**) and $[Ir]_2(HDMA)_2[\beta\text{-}Mo_8O_{26}]\cdot 2DMF\cdot H_2O$ ($HDMA^+$ = dimethylammonium) (**Ir$_2$βMo$_8$HDMA**). These systems differ by the composition and the topology of the POMs, the $[Ir]^+$/POM ratio, the nature of the other counter-cations, and the presence or not of crystallized solvent molecules. Their crystal structures and their photoluminescent properties have been determined and compared with those of a previously reported series of $[Ir]^+$/POM assemblies revealing polymorphism and structural filiations. The emission properties of the compounds are strongly modulated by the nature of the POM units and the crystal packing of the hybrid frameworks.

1. INTRODUCTION

Cyclometalated iridium(III) complexes have attracted much attention in the last decades due to their numerous potential applications for organic light emitting diodes,[1] biological phosphorescent probes,[2] photodynamic therapy agents,[3] catalytic hydrogen photogeneration,[4] light-emitting electrochemical cells,[5] and dye-sensitized solar cells.[6] Among them, heteroleptic cationic iridium complexes $[Ir^{III}(C\text{^}N)_2(N\text{^}N)]^+$ incorporating both cyclometalating (C^N) and ancillary diimine (N^N) ligands have been largely studied because they exhibit highly tunable photophysical properties. In particular, their luminescence is governed by two emitting states e.g., a mixed metal-to-ligand charge transfer (^{3}MLCT) and ligand-to-ligand charge transfer (^{3}LLCT) triplet level, and a ligand-centered ($^3LC_{C\text{^}N}$) second triplet level, whose energies can be finely modulated with the

nature of the ligands.[7] Indeed, the emission wavelength of such systems can be tuned from blue to near-infrared by specific functionalization of both C^N and N^N ligands with electron-withdrawing or electron-donating substituents,[3,8] while an extension of the π-conjugation of the ligands efficiently tunes the emission lifetime of the cationic Ir(III) complexes.[9]

Alternatively, a slight modulation of the solid-state emission properties of a cationic Ir(III) complex from its simple ionic association with classical anions (Cl^-, ClO_4^-, PF_6^-, BPh_4^-) was reported.[10] In marked contrast, we recently evidenced that the emission of the archetypal $[Ir^{III}(ppy)_2(bpy)]^+$ (ppy = 2-phenylpyridine, bpy = 2,2'-bipyridine) complex, hereafter labbelled as $[Ir]^+$ (Figure 1), can be drastically modulated by its supramolecular association with various polyoxometalates (POMs).[11] POMs are considered as nanosized molecular metal-oxide anions. They are built from the connection of $\{MO_x\}$ polyhedra, M being a d-block element in high oxidation state ($V^{IV,V}$, $Mo^{V,VI}$, W^{VI}), possess a wide range of sizes, shapes and charges, and exhibit various properties from catalysis,[12,13] medecine[14,15] to magnetism.[16,17,18] Furthermore their functionalization by grafted or ionically associated organic moieties[19] enlarge the scope of applications[20] to for example molecular electronic,[21] photochromism[22,23,24] or surface anchoring.[25] Our recent investigation of the $[Ir]^+$/POM system led to the elaboration of five hybrid crystallized assemblies, namely $[Ir]_2(TBA)_2[\beta\text{-}Mo_8O_{26}]$-A, $[Ir]_2(TBA)_2[\beta\text{-}Mo_8O_{26}]$-B, $[Ir]_4[\alpha\text{-}Mo_8O_{26}]$, $[Ir]_2[Mo_4O_{10}(OCH_3)_6]\cdot 2CH_3OH$, and $[Ir]_2[W_6O_{19}]$ (labeled as ***t*-Ir_2W_6-1** in the present work).[11] Strikingly, their solid-state emission energy continuously varies on an on-going basis on 115 nm, from green to yellow, orange, orange-red, and red, whithout any prior ligand functionalization but only by playing with the nature of the POM unit and the crystal packing mode. Such hybrid systems can also exhibit remarkable vapoluminescence properties useful for the detection of selective volatile organic compounds (VOCs), and

thus even in presence of moisture.

The reactivity of the $[Ir]^+$ complex towards POMs is a very versatile system that allows designing a wide range of new other supramolecular assemblies by varying numerous synthesis parameters such as the nature of the POMs used, the $[Ir]^+$/POM ratio, temperature and pressure, as well as the nature of solvents and additional counter-cations. In that context, we have embarked on an intense prospective synthesis work, and we report herein the elaboration, the structural characterization and the physical properties of five new $[Ir]^+$/POM hybrid salts (Figure 1), namely $[Ir]_2[W_6O_{19}]\cdot H_2O$ (***m*-Ir$_2$W$_6$**), $[Ir]_2[W_6O_{19}]$ (***t*-Ir$_2$W$_6$-2**), $[Ir]_2[Mo_6O_{19}]$ (***t*-Ir$_2$Mo$_6$-2**), $[Ir]_4[\alpha\text{-}Mo_8O_{26}]\cdot 4DMF\cdot 5H_2O$ (**Ir$_4$αMo$_8$DMF**) and $[Ir]_2(HDMA)_2[\beta\text{-}Mo_8O_{26}]\cdot 2DMF\cdot H_2O$ (**Ir$_2$βMo$_8$HDMA**).

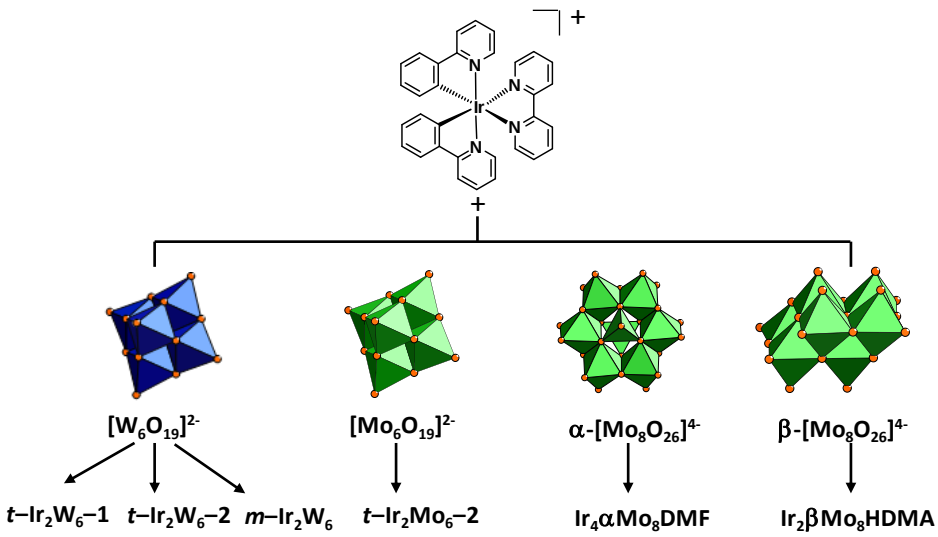

Figure 1. Schematic assemblies of $[Ir^{III}(ppy)_2(bpy)]^+$ ($[Ir]^+$) and POM units in the five new compounds reported in this article and a compound reported previously (blue octahedra = WO_6; green octahedra = MoO_6; green tetrahedra = MoO_4; orange sphere: oxygen).

2. EXPERIMENTAL SECTION

2.1. Synthetic procedures. All chemicals and reagents were purchased from major chemical suppliers and used as received except $[Ir^{III}(ppy)_2(bpy)](PF_6)$ (hereafter labelled as $[Ir](PF_6)$),[26] $(TBA)_2[W_6O_{19}]$,[27] $(TBA)_4[\alpha\text{-}Mo_8O_{26}]$ (TBA^+ = tetrabutylammonium

cation),[28] and $[Ir]_2[W_6O_{19}]$ (***t*-Ir$_2$W$_6$-1**)[11] which have been synthesized according to the reported procedures.

*2.1.1. Synthesis of $[Ir]_2[W_6O_{19}]\cdot H_2O$ (**m-Ir$_2$W$_6$**).* $(TBA)_2[W_6O_{19}]$ (0.173 g, 0.091 mmol) was dissolved in acetonitrile (7 mL). The colourless solution (solution 1) was stirred for a few minutes at room temperature. In addition, a second solution (solution 2) is obtained by dissolving $[Ir](PF_6)$ (0.150 g, 0.187 mmol) in acetonitrile (4 mL) at room temperature. Solution 2 was added dropwise to solution 1 under vigorous stirring leading to the precipitation of an orange solid. The mixture was stirred at 40°C for four hours, kept at room temperature, and then filtered. The powder was washed with acetonitrile, ethanol, and dried in air. Then the powder was dissolved in DMF (3 mL). The resulting orange solution was stirred at 50°C for one hour and the system was setting to standby at ambient temperature. Single-crystals of ***m*-Ir$_2$W$_6$** were obtained after few days. Yield in W: 80%. Anal. Calcd for $C_{64}H_{50}O_{20}N_8W_6Ir_2$: C, 28.04 ; H, 1.80 ; N, 4.09. Found: C, 28.41; H, 1.75; N, 4.01. FT-IR (KBr cm^{-1}): 3101 (w), 3069 (m), 3040 (w), 2972 (w); $[Ir]^+$ complex 1603 (s), 1582 (s), 1560 (w), 1549 (w), 1477 (s), 1443 (s), 1418 (s), 1312 (m), 1267 (m), 1250 (w), 1225 (w), 1163 (s), 1124 (w), 1103 (w), 1063 (m), 1043 (sh), 1032 (m); νW=O, νW-O-W 970 (vs), 893 (w), 880 (sh), 816 (vs), 760 (vs), 748 (s), 733 (s), 669 (m), 638 (sh), 631 (w), 586 (s), 559 (sh), 446 (vs), 420 (m).

*2.1.2. Synthesis of $[Ir]_2[W_6O_{19}]$ (**t-Ir$_2$W$_6$-2**).* $(TBA)_2[W_6O_{19}]$ (0.029 g, 0.015 mmol) was dissolved in acetonitrile (2 mL). The colourless solution (solution 1) was stirred for a few minutes at room temperature. In addition, a second solution (solution 2) is obtained by dissolving $[Ir](PF_6)$ (0.025 g, 0.031 mmol) in acetonitrile (2 mL) at room temperature. Solution 2 was added dropwise to solution 1 under vigorous stirring leading to the precipitation of an orange solid. The resulting yellow solution was sealed in a 30 mL Teflon-lined autoclave and was maintained at 150°C for 40 hours in autogenous pressure

conditions. The reactor was then cooled at room temperature and the microcrystallized orange powder was then filtered, washed with acetonitrile, ethanol, and dried in air. Yield in W: 61%. Anal. Calcd for $C_{64}H_{48}O_{19}N_8W_6Ir_2$: C, 28.25; H, 1.78; N, 4.12. Found: C, 28.25 ; H, 1.73 ; N, 3.88. FT-IR (KBr cm^{-1}): 3101 (w), 3069 (m), 3040 (w), 2972 (w); $[Ir]^+$ complex 1605 (s), 1583 (s), 1561 (w), 1548 (w), 1477 (s), 1443 (s), 1418 (s), 1313 (m), 1270 (m), 1244 (w), 1228 (w), 1157 (s), 1121 (w), 1104 (w), 1062 (m), 1043 (sh), 1032 (m); νW=O, νW-O-W 976 (vs), 887 (w), 816 (vs), 766 (m), 754 (s), 731 (m), 667 (w), 629 (sh), 584 (s), 555 (sh), 446 (vs), 420 (m).

*2.1.3. Synthesis of $[Ir]_2[Mo_6O_{19}]$ (**t-Ir_2Mo_6-2**).* $(TBA)_4[\alpha\text{-}Mo_8O_{26}]$ (0.067 g, 0.031 mmol) was dissolved in acetonitrile (4 mL). The colourless solution (solution 1) was stirred for a few minutes at room temperature. In addition, a second solution (solution 2) is obtained by dissolving $[Ir](PF_6)$ (0.100 g, 0.125 mmol) in acetonitrile (4 mL) at room temperature. Solution 2 was added dropwise to solution 1 under vigorous stirring leading to the precipitation of an orange solid. The mixture was stirred at 35 °C for three hours, kept at room temperature, and then filtered. Single-crystals of ***t*-Ir_2Mo_6-2** were obtained after few days by slow diffusion of ethanol into the solution. Yield in Mo: 45%. Anal. Calcd for $C_{64}H_{48}O_{19}N_8Mo_6Ir_2$: C, 28.04; H, 1.80; N, 4.09. Found: C, 28.41; H, 1.75; N, 4.01. FT-IR (KBr cm^{-1}): 3102 (w), 3067 (m), 3042 (w), 2972 (w); $[Ir]^+$ complex 1605 (s), 1583 (s), 1562 (w), 1549 (w), 1477 (s), 1445 (s), 1418 (s), 1313 (m), 1269 (m), 1245 (w), 1226 (w), 1159 (s), 1124 (w), 1103 (w), 1063 (m), 1043 (sh), 1031 (m); νMo=O, νMo-O-Mo 955 (vs), 883 (sh), 800 (vs), 600 (w), 439 (m).

*2.1.4. Synthesis of $[Ir]_4[\alpha\text{-}Mo_8O_{26}]\cdot 4DMF\cdot 5H_2O$ (**$Ir_4\alpha Mo_8DMF$**).* $(TBA)_4[\alpha\text{-}Mo_8O_{26}]$ (0.067 g, 0.031 mmol) was dissolved in acetonitrile (4 mL). The colourless solution (solution 1) was stirred for a few minutes at room temperature. In addition, a second solution (solution 2) is obtained by dissolving $[Ir](PF_6)$ (0.099 g, 0.124 mmol) in

acetonitrile (4 mL) at room temperature. Solution 2 was added dropwise to solution 1 under vigorous stirring leading to the precipitation of an orange solid of $[Ir]_4[\alpha\text{-}Mo_8O_{26}]\cdot 5CH_3CN$. The mixture was stirred at 35 °C for three hours, kept at room temperature, and then filtered. The powder was then washed with acetonitrile, ethanol, and dried in air. Then the powder was dissolved in DMF (3 mL). The resulting orange solution was stirred at 50°C for one hour and the system was set to standby at ambient temperature. Single-crystals of **$Ir_4\alpha Mo_8$DMF** were obtained after few days. Yield in Mo: 69%. Anal. Calcd for $C_{140}H_{134}O_{35}N_{20}Mo_8Ir_4$: C, 40.01; H, 3.19; N, 6.68. Found: C, 39.83; H, 3.12; N, 6.51. FT-IR (KBr cm^{-1}): 3102 (w), 3067 (m), 3042 (w), 2972 (w); DMF 1659 (vs); $[Ir]^+$ complex 1607 (s), 1582 (s), 1562 (w), 1549 (w), 1477 (s), 1439 (s), 1418 (s), 1387 (m), 1311 (m), 1269 (m), 1248 (w), 1227 (w), 1161 (s), 1124 (w), 1097 (w), 1063 (m), 1043 (sh), 1030 (m); νMo=O, νMo-O-Mo 942 (vs), 922 (vs), 910 (vs), 847 (m), 808 (s), 796 (s), 764 (s), 731 (m), 711 (w), 660 (s), 631 (w), 557 (m), 523 (w), 414 (m).

*2.1.5. Synthesis of $[Ir]_2(HDMA)_2[\beta\text{-}Mo_8O_{26}]\cdot 2DMF\cdot H_2O$ (**$Ir_2\beta Mo_8$HDMA**).* $(TBA)_4[\alpha\text{-}Mo_8O_{26}]$ (0.093 g, 0.043 mmol) and $[Ir](PF_6)$ (0.070 g, 0.087 mmol) were dissolved in DMF (5 mL). The resulting yellow solution was sealed in a 23 mL Teflon-lined autoclave and was then heated to 130°C over a period of 1 h, kept at 130°C for 40 h, and allowed to cool down to room temperature over a period of 36 h. Single-crystals of **$Ir_2\beta Mo_8$HDMA** were obtained after a few days by slow evaporation of the resulting deep green solution. Yield in Mo: 36%. Anal. Calcd for $C_{78}H_{88}O_{31}N_{12}Mo_8Ir_2$: C, 32.97 ; H, 3.12 ; N, 5.91. Found: C, 34.74 ; H, 3.39 ; N, 5.07. FT-IR (KBr cm^{-1}): 3103 (w), 3068 (w), 2956 (w), 2922 (w); DMF 1668 (m); $[Ir]^+$ complex 1607 (s), 1583 (s), 1562 (w), 1549 (w), 1478 (s), 1446 (w), 1418 (m), 1312 (m), 1269 (m), 1247 (w), 1227 (w), 1165 (m), 1125 (w), 1108 (w), 1065 (m), 1044 (sh), 1032 (m); νMo=O, νMo-O-Mo 941 (vs), 909 (vs), 841 (s), 768 (s), 730 (s), 711 (s), 667 (s), 558 (m), 520 (w).

2.2. Physical Measurements. Elemental analyses of the solids were performed by the "Service de microanalyses ICSN CNRS, in Gif sur Yvette (France). FT-IR spectra were recorded in the 4000-400 cm^{-1} range on a BRUKER Vertex equipped with a computer control using the OPUS software. Differential scanning calorimetry (DSC) and thermogravimetric analysis (TGA) were performed by flowing dry argon with a heating and cooling rate of 5°C/min on a SETARAM TG-DSC 111 between 20 and 800°C. Powder X-ray Diffraction spectra were monitored using a D8 Bruker diffractometer in the Bragg-Brentano geometry, equipped with a front germanium monochromator, a copper anode (Cu*K*-L3 radiation λ=1.540598 Å) and a LynxEye PSD detector. Photoluminescence spectra were recorded on a Jobin-Yvon Fluorolog 3 fluorometer equipped with a CCD camera.

2.3. Crystal structure. Intensity data collections were carried out with a Bruker D8 VENTURE diffractometer equipped with a PHOTON 100 CMOS bidimensional detector using a high brilliance IμS microfocus X-ray Mo Kα monochromatized radiation (λ = 0.71073 Å) for compounds ***m*-Ir_2W_6** (CCDC 1856428) and **$Ir_2\beta Mo_8$HDMA** (CCDC 1856431), and with a Bruker Nonius X8 APEX 2 diffractometer equipped with a CCD bidimensional detector using Mo Kα monochromatized radiation (λ = 0.71073 Å) for compounds ***t*-Ir_2Mo_6-2** (CCDC 1856429) and **$Ir_2\alpha Mo_8$DMF** (CCDC 1856430). The absorption corrections were based on multiple and symmetry-equivalent reflections in the data set using the SADABS program[29] based on the method of Blessing.[30] The structures were solved by direct methods and refined by full-matrix least-squares using the SHELX-TL package.[31] The hydrogen atoms were theoretically located on the basis of the conformation of the supporting atoms. In the structure of ***t*-Ir_2Mo_6-2**, the ppy and bpy ligands are disordered over two positions with site occupancies 0.5 and cannot be discriminated. The N and C disordered atoms of these ligands have been refined isotropically. Crystallographic data are given in Table 1 and the complete data can be found in the cif file as Supporting Information.

Table 1. Crystallographic data

	***m*-Ir$_2$W$_6$**	***t*-Ir$_2$Mo$_6$-2**	**Ir$_4$αMo$_8$DMF**	**Ir$_2$βMo$_8$HDMA**
Empirical formula	$C_{64}H_{48}Ir_2N_8O_{19}W_6$	$C_{64}H_{48}Ir_2Mo_6N_8O_{19}$	$C_{140}H_{124}Ir_4Mo_8N_{20}O_{35}$	$C_{72}H_{70}Ir_2Mo_8N_{11}O_{29}$
Formula weight / g	2720.60	2193.14	4182.90	2705.31
Crystal system	Monoclinic	Trigonal	Triclinic	Orthorhombic
Space group	$P2_1/n$	R-3:H	P-1	$Cmca$
a / Å	8.5394(2)	15.888(1)	13.8382(8)	35.069(2)
b / Å	29.2718(7)	15.888(1)	16.6678(9)	18.8165(8)
c /Å	13.5139(4)	44.379(4)	17.352(1)	14.9093(5)
α / °	90	90	93.699(3)	90
β / °	90.570(1)	90	104.301(3)	90
γ /°	90	120	107.531(2)	90
V / Å^3	3377.8(2)	9703(2)	3656.2(4)	9838.4(7)
Z	2	6	1	4
ρ_{calc} / g cm^{-3}	2.675	2.252	1.900	1.826
μ / mm^{-1}	14.17	5.30	4.37	3.75
Data / Parameters	9872 / 452	6331/ 177	12989 / 950	4451 / 305
R_{int}	0.050	0.032	0.041	0.055
GOF	1.02	1.04	1.13	1.09
R (>2σ(I))	R_1[a] = 0.039	0.066	0.040	0.037
	wR_2 [b]= 0.101	0.175	0.114	0.131

[a] $R_1 = \Sigma||F_o|-|F_c||/\Sigma|F_o|$. [b] $wR_2 = [\Sigma w(F_o^2 - F_c^2)^2/\Sigma w(F_o^2)^2]^{1/2}$

3. RESULTS AND DISCUSSION

3.1. Structural description. [Ir]$_2$[W$_6$O$_{19}$] (*t*-Ir$_2$W$_6$-1), [Ir]$_2$[W$_6$O$_{19}$]·H$_2$O (*m*-Ir$_2$W$_6$) and [Ir]$_2$[Mo$_6$O$_{19}$] (*t*-Ir$_2$Mo$_6$-2).

The previously reported compound ***t*-Ir$_2$W$_6$-1** and the new one ***t*-Ir$_2$Mo$_6$-2** show many structural similarities (Figure 2). In both compounds, the $[Ir]^+$ complexes form an honeycomb-like supramolecular layer in the (*ab*) plane with $[M_6O_{19}]^{2-}$ units (M = W, Mo) localized inside the hexagonal cavities of the $[Ir]^+$ framework (Figure 2a). In the structure of ***t*-Ir$_2$Mo$_6$-2**, the $[Ir]^+$ complexes interact with the POMs via electrostatic

interactions, and the shorter C···O distances (3.23 Å) (Figure S1) are well comparable with the sum of the van der Waals radii of the concerned atoms (3.22 Å). The structure of ***t*-Ir$_2$W$_6$-1** and ***t*-Ir$_2$Mo$_6$-2** mainly differ by the relative positioning of two adjacent $\{[Ir]_2[M_6O_{19}]\}$ layers. In the case of ***t*-Ir$_2$W$_6$-1**, the $\{[Ir]_2[W_6O_{19}]\}$ planes are stacked so that the POMs form supramolecular chains running along the crystallographic *c* axis (Figure 2b). For ***t*-Ir$_2$Mo$_6$-2**, the $\{[Ir]_2[Mo_6O_{19}]\}$ planes are mutually offset and both $[Ir]^+$ and POM units are alternatively aligned along the crystallographic *c* axis (Figure 2c).

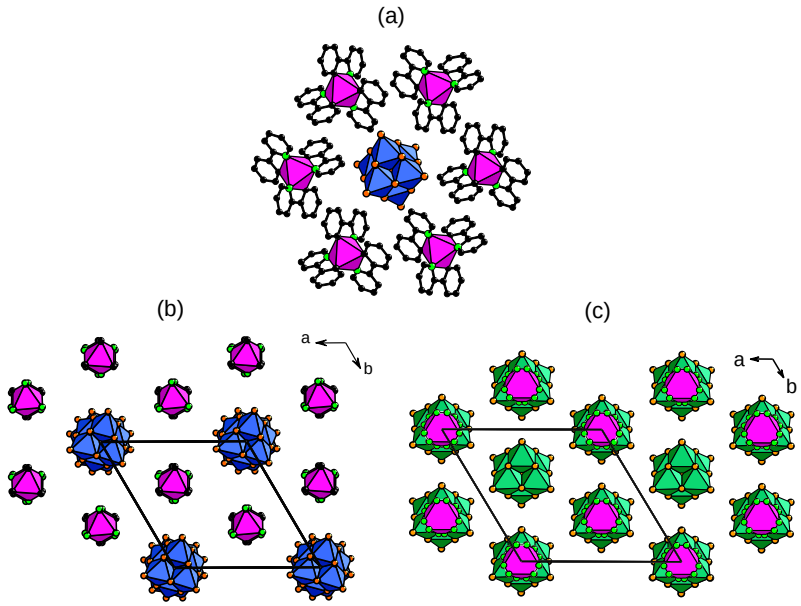

Figure 2. Mixed polyhedral and ball-and-stick representations of the crystal packing in ***t*-Ir$_2$W$_6$-1** and ***t*-Ir$_2$Mo$_6$-2**. (a) Honeycomb-like supramolecular $\{[Ir]_2[M_6O_{19}]\}$ layer (M = W, Mo) (the hydrogen atoms are omitted for clarity). (b) Eclipsed stacking of two adjacent $\{[Ir]_2[W_6O_{19}]\}$ layers in ***t*-Ir$_2$W$_6$-1.** (c) Offset stacking of two adjacent $\{[Ir]_2[Mo_6O_{19}]\}$ layers in ***t*-Ir$_2$W$_6$-2** (only the IrN_xC_y polyedra are displayed for clarity) (blue octahedra = WO_6; green octahedra = MoO_6; magenta octahedra = IrN_xC_y; black spheres: carbon; light-green spheres: nitrogen; orange spheres: oxygen).

In ***m*-Ir$_2$W$_6$**, the honeycomb-like supramolecular $\{[Ir]_2[W_6O_{19}]\}$ layer is much distorted (Figure 3a). This could be due to the additional crystallized water molecules in H-bonding interactions with both the $[Ir]^+$ complexes and the $[W_6O_{19}]^{2-}$ units. The bpy ligand of two $[Ir]^+$ complexes develop strong interactions with the oxygen POM facets with a short

C···O distance of 2.96 Å. The as-defined $\{[Ir]_2[W_6O_{19}]\cdot H_2O\}$ planes display an eclipsed stacking, along the crystallographic *a* axis (Figure 3b).

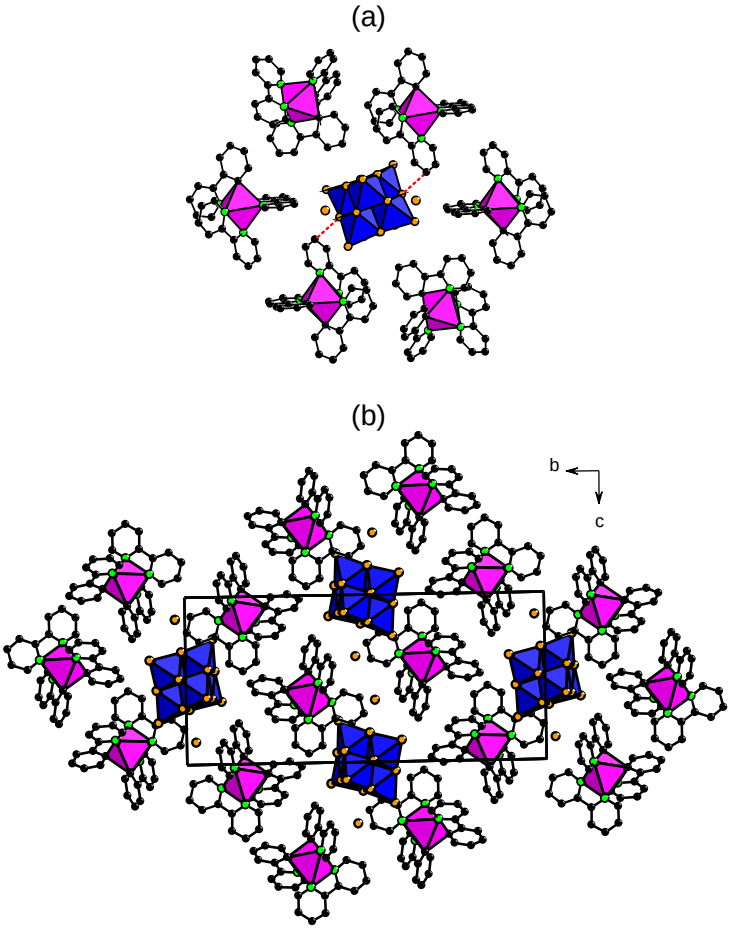

Figure 3. Mixed polyhedral and ball-and-stick representations of the crystal packing in ***m*-Ir_2W_6**. (a) Slightly distorted honeycomb-like supramolecular $\{[Ir]_2[W_6O_{19}]\}$ layer incorporating crystallized water molecules (the hydrogen atoms are omitted for clarity). The shorter C···O distance between the $[Ir]^+$ and POM units are displayed as red dotted lines. (b) Eclipsed stacking of two adjacent $\{[Ir]_2[W_6O_{19}]\cdot H_2O\}$ layers (blue octahedra = WO_6; magenta octahedra = IrN_2C_2; black spheres: carbon; light-green spheres: nitrogen; orange spheres: oxygen).

$[Ir]_2(HDMA)_2[\beta\text{-}Mo_8O_{26}]\cdot 2DMF\cdot H_2O$ (**$Ir_2\beta Mo_8HDMA$**). The crystal structure of **$Ir_2\beta Mo_8HDMA$** is depicted in Figure 4. It contains discrete $\beta\text{-}[Mo_8O_{26}]^{4-}$ entities associated via electrostatic interactions and C-H···O contacts with dimethylammonium ($HDMA^+$) cations and both DMF and water molecules into supramolecular $\{(HDMA)_2[\beta\text{-}Mo_8O_{26}]\cdot 2DMF\cdot H_2O\}^{2-}$ layers in the (bc) plane (Figure 4a). The two $HDMA^+$ cations are

localized on each side of the POM unit and interact with two highly nucleophilic oxo ligands through strong H-bonds (Figure 4b). The $[Ir]^+$ complexes form rectangular paving sheets in the (*bc*) plane (Figure 4c) that are alternatively stacked with the $\{(HDMA)_2[\beta\text{-}Mo_8O_{26}]\cdot 2DMF\cdot H_2O\}^{2-}$ layers along the crystallographic *a* axis (Figure 4d). No π-π overlapping is observed between the ppy and bpy ligands of the $[Ir]^+$ complexes and the oxygen POM facets.

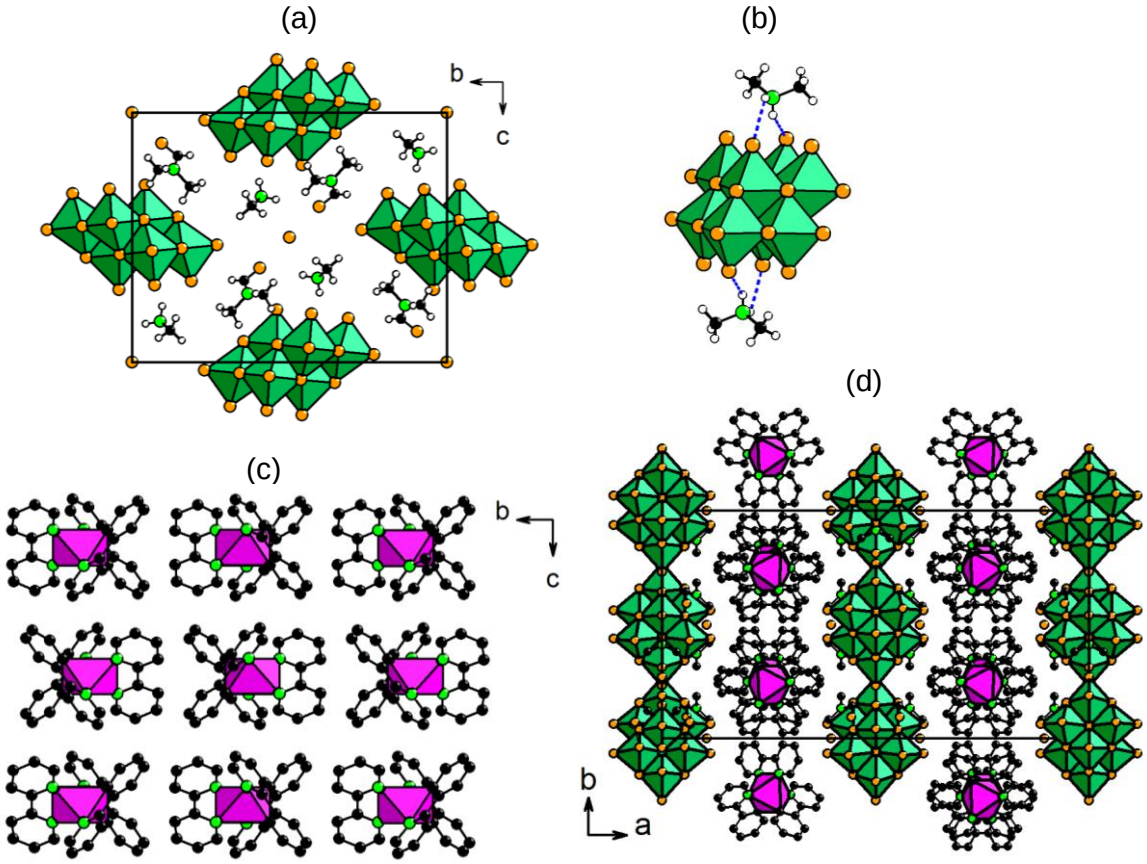

Figure 4. Mixed polyhedral and ball-and-stick representations of the crystal packing in **$[Ir]_2(HDMA)_2[\beta\text{-}Mo_8O_{26}]\cdot 2DMF\cdot H_2O$** displaying (a) the supramolecular $\{(HDMA)_2[\beta\text{-}Mo_8O_{26}]\cdot 2DMF\cdot H_2O\}^{2-}$ layers (H-atoms of the water molecules are not displayed). (b) H-bonding interactions (blue dotted lines) between the $HDMA^+$ cations and the $\beta\text{-}[Mo_8O_{26}]^{4-}$ unit. (c) Rectangular paving of the $[Ir]^+$ complex sub-network. (d) Staking of both the $[Ir]^+$ sheets and the $\{(HDMA)_2[\beta\text{-}Mo_8O_{26}]\cdot 2DMF\cdot H_2O\}^{2-}$ layers (green octahedra = MoO_6; magenta octahedra = IrN_4C_2; black spheres: carbon; light-green spheres: nitrogen; orange spheres: oxygen). The hydrogen atoms of the $[Ir]^+$ complex are omitted for clarity.

$[Ir]_4[\alpha\text{-}Mo_8O_{26}]\cdot 4DMF\cdot 5H_2O$ ($Ir_4\alpha Mo_8DMF$). The crystal structure of **$Ir_4\alpha Mo_8DMF$** is

depicted in Figure 5. It contains discrete α-$[Mo_8O_{26}]^{4-}$ entities associated via electrostatic interactions and C-H···O contacts with two crystallographically unequivalent $[Ir]^+$ cations (hereafter labeled as $[Ir]^+$_1 and $[Ir]^+$_2) and both DMF and water molecules. The $[Ir]^+$ complexes form supramolecular honeycomb-like ribbons ranging along the crystallographic *b* axis (Figure 5a). The α-$[Mo_8O_{26}]^{4-}$ units and water molecules occupy the hexagonal cavities of the $[Ir]^+$ framework. DMF molecules are localized between the {$[Ir]_4$[α-Mo_8O_{26}]} ribbons that are aligned into supramolecular layers. The bpy ligand of two $[Ir]^+$_1 and two $[Ir]^+$_2 complexes strongly interacts with one α-$[Mo_8O_{26}]^{4-}$ anion via electrostatic interactions with a short C···O distance of 3.20 and 3.13 Å, respectively.

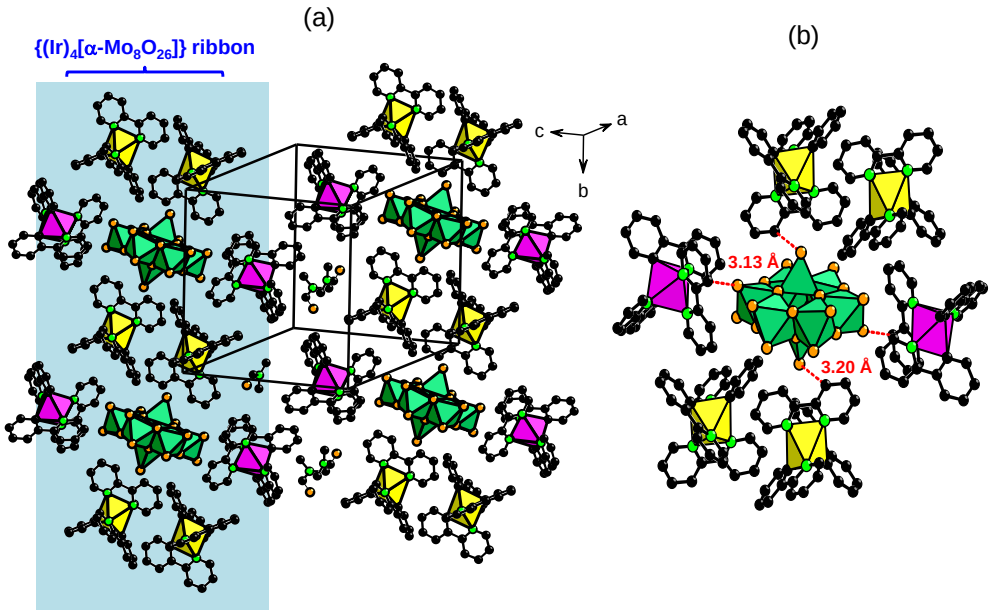

Figure 5. Mixed polyhedral and ball-and-stick representations of the crystal packing in **[Ir]$_4$[α-Mo_8O_{26}]·4DMF·5H_2O**. (a) Supramolecular {$[Ir]_4$[α-Mo_8O_{26}]} ribbons ranging along the *b* axis. Crystallized DMF and water molecules (not shown for clarity) are localized in the space between ribbons. (b) Representation of the direct interactions between the POM unit and the six direct neighboring $[Ir]^+$ complexes. The shorter C···O distance between the $[Ir]^+$ and POM units are displayed as red dotted lines. (green octahedra = MoO_6; yellow octahedra = IrN_4C_2 in $[Ir]^+$_1; magenta octahedra = IrN_4C_2 in $[Ir]^+$_2; black spheres: carbon; green spheres: nitrogen; orange spheres: oxygen). C···O interactions between $[Ir]^+$ complexes and α-$[Mo_8O_{26}]^{4-}$ units are displayed as dotted lines.

3.2. Synthesis. Five new hybrid $[Ir]^+$/POM assemblies have been synthesized by different routes, as displayed in Scheme 1. The assembly of the Lindqvist-type $[W_6O_{19}]^{2-}$ anion with two folds of $[Ir]^+$ in acetonitrile gives rise to a very versatile system containing three different compounds, namely the previously reported trigonal phase $[Ir]_2[W_6O_{19}]\cdot$(***t*-Ir$_2$W$_6$-1**),[11] a new monoclinic phase $[Ir]_2[W_6O_{19}]\cdot H_2O$ (***m*-Ir$_2$W$_6$**), as well as another new trigonal one $[Ir]_2[W_6O_{19}]$ (***t*-Ir$_2$W$_6$-2**) which is a polymorph of ***t*-Ir$_2$W$_6$-1**. Its isostructural molybdenum counterpart $[Ir]_2[Mo_6O_{19}]$ (***t*-Ir$_2$Mo$_6$-2**) was also synthesized from a different synthesis procedure. Crystallized water molecules in ***m*-Ir$_2$W$_6$** have been well evidenced by a combination of FT-IR spectroscopy (Figure S2), elemental analysis and TGA/DSC measurements (Figure S3). ***m*-Ir$_2$W$_6$**, ***t*-Ir$_2$W$_6$-1** and ***t*-Ir$_2$W$_6$-2** were obtained by varying temperature and pressure conditions (Scheme 2). Syntheses were carried out under ambient pressure for temperature ranging from 40°C to 100°C while solvothermal conditions were used for temperatures above 100°C. The powder X-ray diffraction (PXRD) analysis reveals that the orange solid obtained at 40°C contains a mixture of ***t*-Ir$_2$W$_6$-1** with a small amount of ***m*-Ir$_2$W$_6$** (Figure 6a). Its formation could be due to the presence of a small quantity of water probably due to a moist environment. Strikingly, after dissolving the as-obtained mixed powder in DMF, pure crystals of each of the two phases can be separately obtained with good yield from different crystallization techniques. Orange crystals of ***m*-Ir$_2$W$_6$** were isolated by setting to standby the DMF solution in ambient conditions for a few days, while pure orange-red crystals of ***t*-Ir$_2$W$_6$-1** were obtained by slow diffusion of anhydrous ethanol into the solution. When the initial reaction was carried out by using temperatures ranging from 60°C to 150°C, the ***m*-Ir$_2$W$_6$** phase disappears and the obtained orange solid was a mixture of both ***t*-Ir$_2$W$_6$-1** and ***t*-Ir$_2$W$_6$-2** (Figure 6b). Finally for temperatures ranging from 150°C to 180°C, only the ***t*-Ir$_2$W$_6$-2** phase was obtained purely as a microcrystalline orange powder (Figure 6c).

Attempts to isolate single crystals were unsuccessful. However the comparison of the experimental PXRD pattern of ***t*-Ir$_2$W$_6$-2** with that calculated from the structure of its Mo counterpart ***t*-Ir$_2$Mo$_6$-2** solved from single-crystal X-ray diffraction data (Figure S4) has allowed to confirm that both compounds are isostructural. As discussed in section 3.1, the structures of the two polymorphous phases ***t*-Ir$_2$W$_6$-1** and ***t*-Ir$_2$W$_6$-2** mainly differ by an offset of the supramolecular {[Ir]$_2$[Mo$_6$O$_{19}$]} layers stacked along the *c* axis, which at first sight could be induced by increasing the temperature.

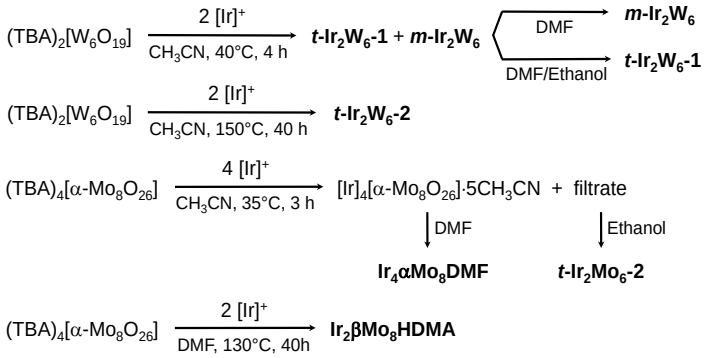

Scheme 1 Synthetic routes to the new [Ir]$^+$/POM assemblies.

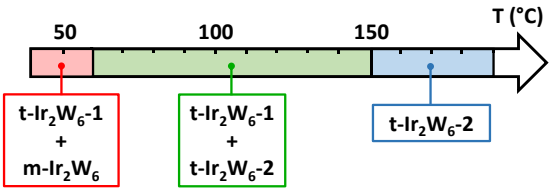

Scheme 2

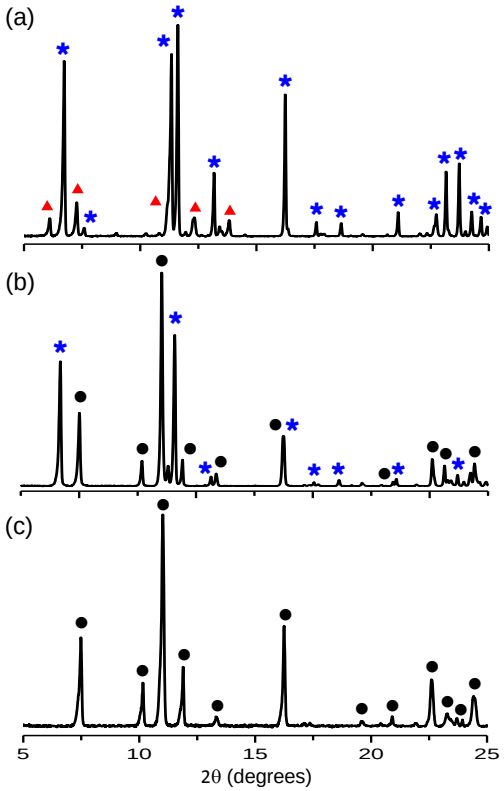

Figure 6. PXRD patterns of hybrid systems obtained from $(TBA)_2[W_6O_{19}]$ and two folds of $[Ir](PF_6)$ in acetonitrile at the synthesis temperature of (a) 40°C, (b) 60°C and (c) 150°C. Peaks labeled with blue stars, red triangles and black circles, are assigned to ***t*-Ir$_2$W$_6$-1**, ***m*-Ir$_2$W$_6$** and ***t*-Ir$_2$W$_6$-2**, respectively.

Ir$_4$αMo$_8$DMF and **Ir$_2$βMo$_8$HDMA** were obtained during the investigation of the $[Ir]^+$/α-$[Mo_8O_{26}]^{4-}$ system by using $[Ir]^+$:$[Mo_8O_{26}]^{4-}$ ratios of 4:1 and 2:1, respectively. **Ir$_4$αMo$_8$DMF** was synthesized from a two step procedures. First, an orange powder of the hybrid compound $[Ir]_4[\alpha\text{-}Mo_8O_{26}]\cdot 5CH_3CN$ was isolated with high yield by mixing $(TBA)_4[\alpha\text{-}Mo_8O_{26}]$ with four equivalents of $[Ir](PF_6)$ in acetonitrile. The FT-IR spectrum of $[Ir]_4[\alpha\text{-}Mo_8O_{26}]\cdot 5CH_3CN$ (Figure S5) revealed the presence of the discrete α-$[Mo_8O_{26}]^{4-}$ unit while elemental analysis and TGA/DSC measurements indicated an $[Ir]^+$:$[Mo_8O_{26}]^{4-}$:CH_3CN ratio of 4:1:5 (Figure S6). Attempts to isolate single-crystals of this intermediary phase were unsuccessful. In a second step, single crystals of **Ir$_4$αMo$_8$DMF** were obtained by dissolving the powder of $[Ir]_4[\alpha\text{-}Mo_8O_{26}]\cdot 5CH_3CN$ in

DMF, and setting to standby the solution at ambient temperature for a few days. The presence of the α-$[Mo_8O_{26}]^{4-}$ unit in **Ir4αMo8DMF** was quite confirmed by FT-IR spectroscopy (Figure S5). Interestingly, as displayed in Figure 7, a structural filiation can be established between **Ir4αMo8DMF** and the previously reported assembly **$[Ir]_4[\alpha\text{-}Mo_8O_{26}]$** (**Ir4αMo8**) which does not contain any crystallized solvent molecules.[11] This compound was obtained following a synthesis procedure similar to that described above but using solvothermal conditions (100°C, 24h). Experimentally, the powder of **Ir4αMo8DMF** can be thermally converted to **Ir4αMo8** by heating at 100°C for few hours, which promotes the removal of crystallized solvent molecules. As described in section 3.1, **Ir4αMo8DMF** is built upon supramolecular {$[Ir]_4[\alpha\text{-}Mo_8O_{26}]$} ribbons ranging along the *b* axis. Due to the presence of crystallized DMF and water molecules, the ribbons are offset such that three $[Ir]^+$ complexes of two neighboring ribbons form a highly distorted hexagon containing the solvent molecules (Figure 7a). Their removal during the conversion from **Ir4αMo8DMF** to **Ir4αMo8** leads to a realignment of the ribbons along the *b* axis such that the six $[Ir]^+$ complexes define a perfect hexagon (Figure 7b).

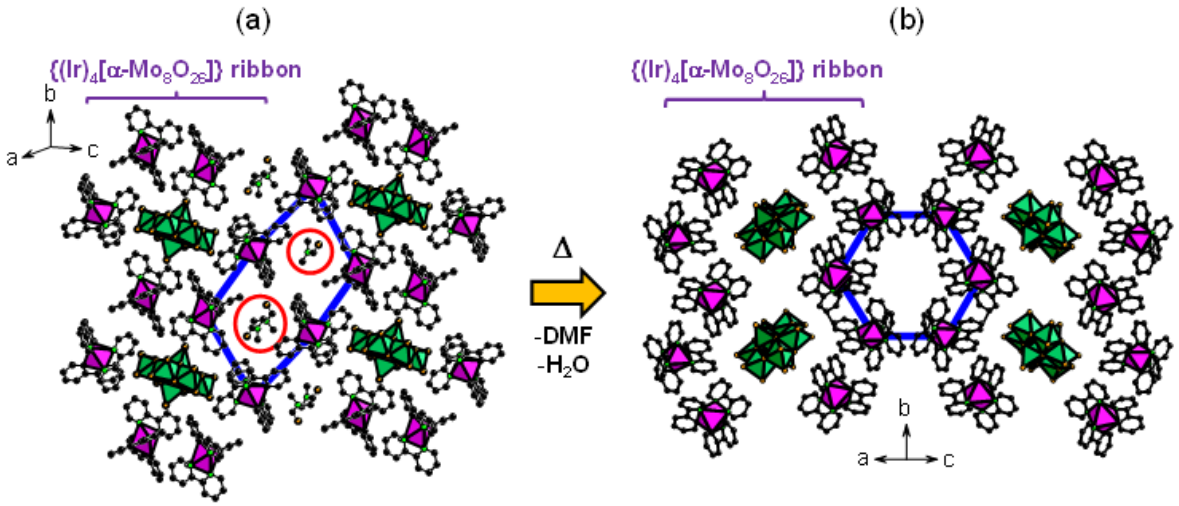

Figure 7. Schematic structural filiation between (a) **$[Ir]_4[\alpha\text{-}Mo_8O_{26}]\cdot 4DMF\cdot 5H_2O$** and (b) **$[Ir]_4[\alpha\text{-}Mo_8O_{26}]$**.[11] The crystallized water (not shown here) and DMF molecules (in red circles) in **$[Ir]_4[\alpha\text{-}Mo_8O_{26}]\cdot 4DMF\cdot 5H_2O$**

are localized inside a strongly distorted hexagonal cavity (blue line) formed by three $[Ir]^+$ complexes of two neighboring supramolecular $\{[Ir]_4[\alpha\text{-}Mo_8O_{26}]\}$ ribbons. After removing the solvent molecules, the $\{[Ir]_4[\alpha\text{-}Mo_8O_{26}]\}$ ribbons realign along the *b* axis and the six $[Ir]^+$ complexes define a perfect hexagonal cavity (blue line) (green octahedra = MoO_6; magenta octahedra = IrN_4C_2; black spheres: carbon; green spheres: nitrogen; orange spheres: oxygen). Hydrogen atoms are omitted for clarity.

$Ir_2\beta Mo_8$HDMA was also obtained from a DMF solution containing $(TBA)_4[\alpha\text{-}Mo_8O_{26}]$ and two folds of $[Ir](PF_6)$, and by using solvothermal conditions (130°C - 40h). Both structural and elemental analyses quite confirmed that the initial $[Ir]^+$:$[Mo_8O_{26}]^{4-}$ ratio of 2:1 is maintained in **$Ir_2\beta Mo_8$HDMA**. The negative charge of the β-$[Mo_8O_{26}]^{4-}$ unit is then compensated by two $HDMA^+$ cations. Their formation results from the thermally-activated hydrolysis of DMF which could be catalyzed by the POM.[32] The crystal packing in **$Ir_2\beta Mo_8$HDMA** shows strong similarities with that observed in our previously reported assembly $(Ir)_2(TBA)_2[\beta\text{-}Mo_8O_{26}]$-B[11] (Figure S7). Interestingly, the nature of the counter-cations impacts the topology of the octamolybdate anion in **$Ir_4\alpha Mo_8$DMF** and **$Ir_2\beta Mo_8$HDMA**. **$Ir_4\alpha Mo_8$DMF** contains the α-$[Mo_8O_{26}]^{4-}$ unit associated with four $[Ir]^+$ complexes while in **$Ir_2\beta Mo_8$HDMA** the β-$[Mo_8O_{26}]^{4-}$ form is connected to two $[Ir]^+$ complexes and two small $HDMA^+$ cations. This is in direct line with previous reports showing that the less compacted α-$[Mo_8O_{26}]^{4-}$ isomer is better stabilized when associated with only large counter-cations, while the more compacted β-$[Mo_8O_{26}]^{4-}$ isomer is rather favored in the presence of small counter-cations able to develop strong H-bonding networks with the POM unit.[33,34]

3.3. Luminescence Properties. Figure 8a displays the room temperature steady-state photoluminescence (PL) spectra of ***m*-Ir_2W_6**, ***t*-Ir_2W_6-1**, and ***t*-Ir_2W_6-2** as well as their colorimetric coordinates in the CIE (Commission Internationale de l'Eclairage) color

space chromaticity diagram. Under UV excitation (λ_{ex} = 365 nm), ***t*-Ir_2W_6-1** is an orange-red emitter characterized by a broad featureless band peaking at 621 nm which was attributed to an emission resulting from the ^{3}MLCT/^{3}LLCT triplet level.[11] The PL spectrum of ***m*-Ir_2W_6** displays a similar broad structureless emission band at 614 nm. Its colorimetric coordinates are very close to those of ***t*-Ir_2W_6-1** but the emission color of ***m*-Ir_2W_6** is slightly shifted to orange due to the presence of an additional shouldered emission band at 522 nm. At first sight, we may assume that this latter could be assigned to a minor emission process resulting for the second ^{3}LC triplet level of the $[Ir]^+$ complex which is much more marked in ***m*-Ir_2W_6** than in ***t*-Ir_2W_6-1**. As discussed in section 3.1, the structure of ***m*-Ir_2W_6** mainly differs from that of ***t*-Ir_2W_6-1** by a slight deformation of the honeycomb-like supramolecular $\{[Ir]_2[W_6O_{19}]\}$ layers due to the presence of additional crystallized water molecules in close proximity to the POM units. Without being negligible, this modulation in the crystal packing has a limited impact on the overall emission energy of the $[Ir]^+$ complex which remains close in both systems. In marked contrast, the PL properties of ***t*-Ir_2W_6-2** strongly differ from those of its polymorph ***t*-Ir_2W_6-1**. ***t*-Ir_2W_6-2** exhibits a yellow-orange emission color, and its PL spectrum displays both a narrow band at 535 nm and less intense broader bands peaking at about 594 nm, which should be indicative of dual emission processes from the two excited triplet levels of the $[Ir]^+$ complex. Attempt to clearly correlate this modulation with structural parameters is not trivial because the structures of both polymorphs differ by the relative positioning of the honeycomb-like supramolecular $\{[Ir]_2[W_6O_{19}]\}$ layers but also by the orientation of the $[Ir]^+$ complexes which are disordered over two positions in ***t*-Ir_2W_6-2**. Nevertheless, as already reported for $[Ir]_2(TBA)_2[\beta\text{-}Mo_8O_{26}]$-A and $[Ir]_2(TBA)_2[\beta\text{-}Mo_8O_{26}]$-B,[11] these results clearly underline again that for hybrid polymorphous systems containing the same POM units, the topology of the framework can strongly impact their

luminescence properties.

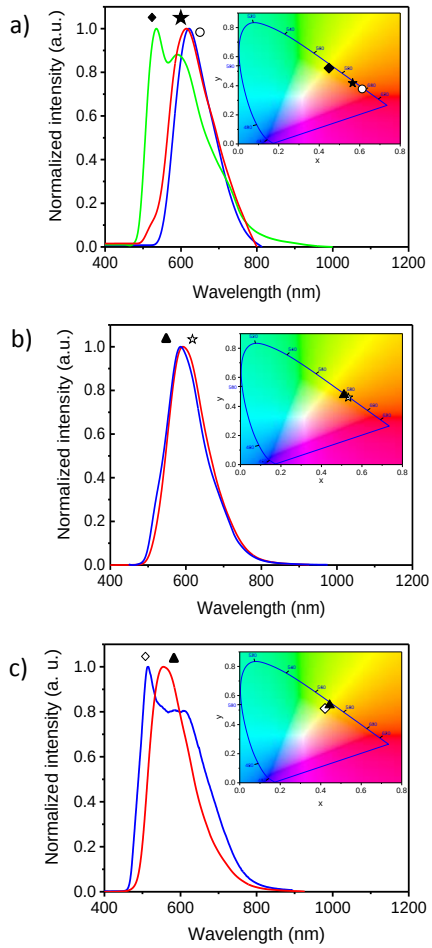

Figure 8. Room-temperature steady-state photoluminescent spectra and colorimetric coordinates (inset) of (a) ***t*-Ir_2W_6-1** (○), ***m*-Ir_2W_6** (★), and ***t*-Ir_2W_6-2** (♦), (b) **$Ir_4\alpha Mo_8$DMF** (▲) and **$Ir_4\alpha Mo_8$** (☆), and (c) $(Ir)_2(TBA)_2$[β-Mo_8O_{26}]-B (◊) and **$Ir_2\beta Mo_8$HDMA** (▲).

The PL spectra of **$Ir_4\alpha Mo_8$DMF** (Figure 8b) shows a broad symmetrical emission band located at 587 nm which is quite comparable with that observed for **$Ir_4\alpha Mo_8$** (λ_{em} = 594 nm),[11] and both compounds exhibit quasi-similar colorimetric coordinates. This could be explained considering that these two hybrid systems are built upon very similar supramolecular {$[Ir]_4[\alpha$-$Mo_8O_{26}]$} ribbons (Figure 7), and that the crystallized solvent molecules localized between the ribbons in **$Ir_4\alpha Mo_8$DMF** do not impact the emission properties of the $[Ir]^+$ entities. Finally the PL properties of **$Ir_2\beta Mo_8$HDMA** were

compared with those of $[Ir]_2(TBA)_2[\beta\text{-}Mo_8O_{26}]$-B (Figure 8c) which shows strong structural similarities (section 3.1). Strikingly, both compouds have very comparable colorimetric coordinates characterizing a similar yellow-orange emission color. The PL spectrum of $[Ir]_2(TBA)_2[\beta\text{-}Mo_8O_{26}]$-B displays both a narrow band at 510 nm and a second broader band centered at about 585 nm which are assigned to both emission processes from the ^{3}LC and the ^{3}MLCT/^{3}LLCT excited triplet levels, respectively.[11] **$Ir_2\beta Mo_8$HDMA** shows a unique unsymmetrical broad band peaking at 558 nm. However the unusual features of this band suggest a contribution of both emission processes with relative intensities different than those observed for $[Ir]_2(TBA)_2[\beta\text{-}Mo_8O_{26}]$-B.

4. CONCLUSION

To summarize, five new phosphorescent hybrid salts associating the cationic cyclometalated $[Ir]^+$ complex with different POM units were successfully synthesized and characterized by single-crystal X-ray diffraction analysis. These compounds well complete a previously reported series of $[Ir]^+$/POM systems,[11] and confirm that this innovative coupling is an efficient strategy to modulate the solid-state photophysical properties of the iridium(III) complexes. Two new compounds ***m*-Ir_2W_6** and ***t*-Ir_2W_6-2** have been obtained from the investigation of the $[Ir]^+/[W_6O_{19}]^{2-}$ system. ***t*-Ir_2W_6-2** is a polymorph of the previously reported ***t*-Ir_2W_6-1**, and their structures mainly differ by two different stacking configurations of the honeycomb-like supramolecular $\{[Ir]_2[M_6O_{19}]\}$ layer, while ***m*-Ir_2W_6** is a hydrated derivative of ***t*-Ir_2W_6-1**. Although the three hybrid compounds contain the same POM unit, their emission color strongly differ due to different contributions of the ^{3}LC and ^{3}MLCT/^{3}LLCT emitting states in the phosphorescence process of the $[Ir]^+$ cation. A structural filiation has been identified between the new compound **$Ir_4\alpha Mo_8$DMF** and the previously reported non-solvated system **$Ir_4\alpha Mo_8$** that can be obtained by heating **$Ir_4\alpha Mo_8$DMF**. Both

compounds are built upon very comparable supramolecular {[Ir]$_4$[α-Mo$_8$O$_{26}$]} ribbons and they exhibit very similar PL properties not impacted by the presence or absence of the crystallized solvent molecules. Finally, the crystal packing of the new hybrid system **Ir$_2$βMo$_8$HDMA** shows strong similarities with that of the already known [Ir]$_2$(TBA)$_2$[β-Mo$_8$O$_{26}$]-B, and both assemblies exhibit very similar emission colors. All these results clearly confrm that the nature of the POM and the topology of the crystal packing have a strong impact on the PL properties of the heteroleptic cationic Ir(III) complexes.

ASSOCIATED CONTENT

Supporting Information: This material is available free of charge via the Internet at http://pubs.acs.org.

Accession codes: Crystallographic data for the new structures reported herein were deposited with the Cambridge Crystallographic Data Centre and allocated the deposition numbers CCDC 1856428-1856431. These data can be obtained free of charge from the Cambridge Crystallographic Data Centre via www.ccdc.cam.ac.uk/data_request/cif.

AUTHOR INFORMATION

Corresponding Authors

*E-mail: anne.dolbecq@uvsq.fr.

*E-mail: remi.dessapt@cnrs-imn.fr

ACKNOWLEDGMENTS

This work was supported by the Ministère de l'Enseignement Supérieur et de la Recherche, the CNRS, the Université de Versailles Saint Quentin en Yvelines, the Université de Nantes,

the LUMOMAT project supported by the Région des Pays de la Loire and a public grant overseen by the French National Research Agency (ANR) as part of the “Investissements d’Avenir” program n°ANR-11-IDEX-0003-02 and CHARMMMAT ANR-11-LABX-0039.

REFERENCES

SYNOPSIS FOR TABLE OF CONTENTS

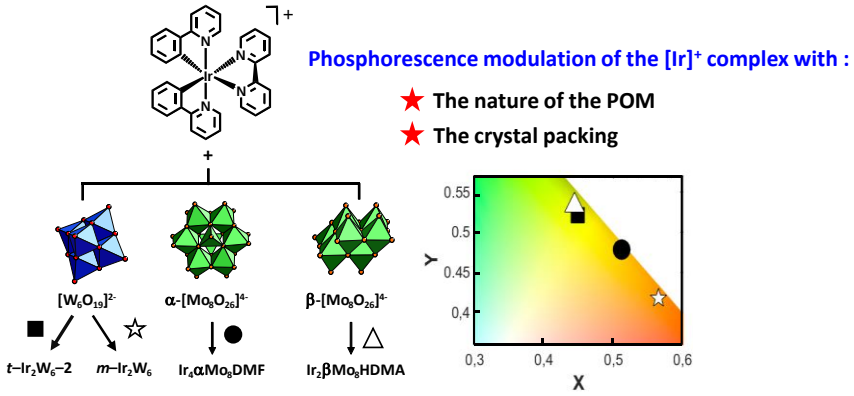

The structure of ionic compounds associating polyoxometalates and Ir(III) complexes has been modulated by using different POMs under various synthetic conditions. The photoluminescence properties of these assemblies depend on their composition and structure.

([1]) Lamansky, S.; Djurovich, P.; Murphy, D.; Abdel-Razzaq, F.; Lee, H.; Adachi, C.; Burrows, P. E.; Forrest, S. R.; Thompson, M. E. Highly phosphorescent bis-cyclometalated iridium complexes: synthesis, photophysical characterization, and use in organic light emitting diodes. *J. Am. Chem. Soc*. **2001**, *123*, 4304-4312.

([2]) Lo, K. K.-W. ; Chan, B. T.-N.; Liu, H.-W.; Zhang, K. Y.; Li, S. P.-Y.; Tang, T. S.-M. Cyclometalated iridium(III) polypyridine dibenzocyclooctyne complexes as the first phosphorescent bioorthogonal probes. *Chem. Commun*. **2013**, *49*, 4271-4273.

([3]) Wang, F.-X. ; Chen, M.-H.; Lin, Y.-N.; Zhang, H.; Tan, C.-P.; Ji, L.-N.; Mao, Z. Dual Functions of Cyclometalated Iridium(III) Complexes: Anti-Metastasis and Lysosome-Damaged Photodynamic Therapy. *ACS Appl. Mater. Interfaces* **2017**, *9*, 42471-42481.

([4]) Yuan, Y.-J. ; Zhang, J.-Y. ; Yu, Z.-T. ; Feng, J.-Y. ; Luo, W.-J. ; Ye, J.-H. ; Zou, Z.-G. Impact of ligand modification on hydrogen photogeneration and light-harvesting applications using cyclometalated iridium complexes. *Inorg. Chem*. **2012**, *51*, 4123-4133.

([5]) Su, H.-C.; Chen, H.-F.; Fang, F.-C.; Liu, C.-C.; Wu, C.-C.; Wong, K.-T.; Liu, Y.-H.; Peng, S.-M. Solid-State White Light-Emitting Electrochemical Cells Using Iridium-Based Cationic Transition Metal Complexes. *J. Am. Chem. Soc* **2008**, *130*, 3413-3419.

([6]) Baranoff, E.; Yum, J.-H.; Jung, I.; Vulcano, R.; Gratzel, M.; Nazeeruddin, M. K. Cyclometallated Iridium Complexes as Sensitizers for Dye-Sensitized Solar Cells. *Chem. Asian J*. **2010**, *5*, 496-499.

([7]) De Angelis, F.; Fantacci, S.; Evans, N.; Klein, C.; Zakeeruddin, S. M.; Moser, J.-E.; Kalyanasundaram, K.; Bolink, H. J.; Gratzel, M.; Nazeeruddin, M. K. Controlling phosphorescence color and quantum yields in cationic iridium complexes: a combined experimental and theoretical study. *Inorg. Chem*. **2007**, *46*, 5989-6001.

([8]) Tamayo, A. B.; Garon, S.; Sajoto, T.; Djurovich, P. I.; Tsyba, I. M.; Bau, R.; Thompson, M. E. Cationic bis-cyclometalated iridium(III) diimine complexes and their use in efficient blue, green, and red electroluminescent devices. *Inorg. Chem*. **2005**, *44*, 8723-8732.

([9]) Zhao, Q.; Yu, M.; Shi, L.; Liu, S.; Li, C.; Shi, M.; Zhou, Z.; Huang, C.; Li, F. Cationic Iridium(III) Complexes with Tunable Emission Color as Phosphorescent Dyes for Live Cell Imaging. *Organometallics* **2010**, *29*, 1085-1091.

([10]) Talarico, A. M.; Ildyko Szerb, E.; Mastropietro, T. F.; Aiello, I.; Crispini, A.; Ghedini, M. Tuning solid state luminescent properties in a hydrogen bonding-directed supramolecular assembly of bis-cyclometalated iridium(III) ethylenediamine complexes. *Dalton Trans.* **2012**, *41*, 4919-4926.

([11]) Bolle, P.; Serier-Brault, H.; Génois, R.; Faulques, E.; Boulmier, A.; Oms, O.; Lepeltier, M.; Marrot, J.; Dolbecq, A.; Mialane, P.; Dessapt, R. Drastic solid-state luminescence color tuning of an archetypal Ir(III) complex using polyoxometalates and its application as a vapoluminescence chemosensor. *J. Mater. Chem. C* **2016**, *4*, 11392-11395.

([12]) Wang, S.-S.; Yang, G.-Y. Recent Advances in Polyoxometalate-Catalyzed Reactions. *Chem. Rev*. **2015**, *115*, 4893-4962.

([13]) Lechner, M.; Güttel, R.; Streb, C. Challenges in polyoxometalate-mediated aerobic oxidation catalysis: catalyst development meets reactor design. *Dalton Trans*. **2016**, *45*, 16716-16726.

([14]) Bijelic, A.; Aureliano, M.; Rompel, A. The antibacterial activity of polyoxometalates: structures, antibiotic effects and future perspectives. *Chem. Commun*. **2018**, *54*, 1153-1169.

([15]) Bijelic, A.; Aureliano, M.; Rompel, A. Polyoxometalates as potential next-generation metallodrugs in the combat against cancer. *Angew. Chem., Int. Ed. Engl*., DOI:10.1002/anie.201803868.

([16]) Clemente-Juan, J.; Coronado, E.; Gaita-Ariño, A. *Chem. Soc. Rev*. **2012**, *41*, 7464-7478.

([17]) Zheng, S.-T.; Yang, G.-Y. Recent advances in paramagnetic-TM-substituted polyoxometalates (TM = Mn, Fe, Co, Ni, Cu) *Chem. Soc. Rev*. **2012**, *41*, 7623-7646.

([18]) Ma, P.; Hu, F.; Huo, Y.; Zhang, D. ; Zhang, C. ; Niu, J. ; Wang, J. Magnetoluminescent Bifunctional Dysprosium-Based Phosphotungstates with Synthesis and Correlations between Structures and Properties. *Cryst. Growth Des*. **2017**, *17*, 1947-1956.

([19]) Dolbecq, A.; Dumas, E.; Mayer, C. R.; Mialane, P. Hybrid Organic-Inorganic Polyoxometalate Compounds: From Structural Diversity to Applications *Chem. Rev*. **2010**, *110*, 6009-6048.

([20]) Song, Y.-F.; Tsunashima, R. Recent advances on polyoxometalate-based molecular and composite materials. *Chem. Soc. Rev*. **2012**, *41*, 7384-7402.

([21]) Izzet, G.; Volatron, F.; Proust, A. Tailor–made Covalent Organic-Inorganic Polyoxometalate Hybrids: Versatile Platforms for the Elaboration of Functional Molecular Architectures. *Chem. Rec*. **2017**, *17*, 250-266.

([22]) Saad, A.; Oms, O.; Dolbecq, A.; Menet, C.; Dessapt, R.; Serier-Brault, H.; Allard, E.; Baczko, K.; Mialane, P. A high fatigue resistant, photoswitchable fluorescent spiropyran–polyoxometalate–BODIPY single-molecule. *Chem. Commun.* **2015**, *51*, 16088–16091.

([23]) Saad, A.; Oms, O.; Marrot, J.; Dolbecq, A.; Hakouk, K.; El Bekkachi, H.; Jobic, S.; Deniard, P.; Dessapt, R.; Garrot, D.; Boukheddaden, K.; Liu, R.; Zhang, G.; Keita, B.; Mialane, P. Design and optical investigations of a spironaphthoxazine/polyoxometalate/spiropyran triad. *J. Mater. Chem. C* **2014**, *2*, 4748-4758.

([24]) Hakouk, K.; Oms, O.; Dolbecq, A.; Marrot, J.; Saad, A.; Mialane, P.; El Bekkachi, H.; Jobic, S.; Deniard, P.; Dessapt, R. New photoresponsive charge-transfer spiropyran/polyoxometalate assemblies with highly tunable optical properties. *J. Mater. Chem. C* **2014**, *2*, 1628-1641.

([25]) Aguado-Ureta, S.; Rodriguez-Hernandez, J.; del Campo, A.; Perez-Alvarez, L.; Ruiz-Rubio, L.; Vilas, J. ; Artetxe, B. ; Reinoso, S. ; Gutierrez-Zorilla, J. M. Immobilization of Polyoxometalates on Tailored Polymeric Surfaces. *Nanomaterials* **2018**, *8*, DOI:10.3390/nano8030142.

([26]) Costa, R. D.; Orti, E.; Bolink, H. J.; Graber, S.; Schaffner, S.; Neuburger, M.; Housecroft, C. E.; Constable, E. C. Archetype Cationic Iridium Complexes and Their Use in Solid-State Light-Emitting Electrochemical Cells. *Adv. Funct. Mater.* **2009**, *19*, 3456-3463.

([27]) Sanchez, C.; Livage, J.; Launay, J. P.; Fournier, M. Electron delocalization in mixed-valence tungsten polyanions. *J. Am. Chem. Soc.* **1983**, *105*, 6817-6823.

([28]) Klemperer, W. G. *Inorg. Synth.* **1990**, *27*, 74-85.

([29]) Sheldrick, G. M. SADABS, program for scaling and correction of area detector data, University of Göttingen, Germany, 1997.

([30]) Blessing, R. An empirical correction for absorption anisotropy. *Acta Crystallogr.* **1995**, *A51*, 33-38.

([31]) Sheldrick, G. M. SHELX-TL version 5.03, Software Package for the Crystal Structure Determination, Siemens Analytical X-ray Instrument Division: Madison, WI USA, 1994.

([32]) Liu, S.; Wang, C.; Zhai, H.; Li, D. Hydrolysis of N,N-dimethylformamide catalyzed by the Keggin $H_3[PMo_{12}O_{40}]$: isolation and crystal structure analysis of $[(CH_3)_2NH_2]_3[PMo_{12}O_{40}]$. *J. Mol. Struct.* **2003**, *654*, 215-221.

([33]) Coué, V.; Dessapt, R.; Bujoli-Doeuff, M.; Evain, M.; Jobic, S. Synthesis and characterization of two new photochromic organic–inorganic hybrid materials based on isopolyoxomolybdate: $(HDBU)_3(NH_4)[\beta\text{-}Mo_8O_{26}]\cdot H_2O$ and $(HDBU)_4[\delta\text{-}Mo_8O_{26}]$. *J. Solid. State Chem.* **2006**, *179*, 3615-3627.

([34]) Klemperer, W.G.; Shum, W. Synthesis and interconversion of the isomeric α- and β-molybdate ($Mo_8O_{26}^{4-}$) ions. *J. Am. Chem. Soc.* **1976**, *98*, 8291-8293.